



## A novel porous coral-like $Zn_{0.5}Ni_{0.5}Co_2O_4$ as an anode material for lithium ion batteries with excellent rate performance

Xiong Song <sup>a, b, c</sup>, Qiang Ru <sup>a, b, c, \*</sup>, Yudi Mo <sup>a, b, c</sup>, Lingyun Guo <sup>a, b, c</sup>, Shejun Hu <sup>a, b, c</sup>, Bonan An <sup>a, b, c</sup>

<sup>a</sup> School of Physics and Telecommunication Engineering, South China Normal University, Guangzhou 510006, PR China

<sup>b</sup> Engineering Research Center of Materials and Technology for Electrochemical Energy Storage (Ministry of Education), Guangzhou 510006, PR China

<sup>c</sup> Laboratory of Quantum Engineering and Quantum Materials, School of Physics and Telecommunication Engineering, South China Normal University, Guangzhou 510006, PR China



### HIGHLIGHTS

- The porous coral-like  $Zn_{0.5}Ni_{0.5}Co_2O_4$  is prepared by co-precipitation method.
- The preparation method has mild experiment conditions and high yield.
- The coral-like  $Zn_{0.5}Ni_{0.5}Co_2O_4$  electrode shows excellent electrochemical performance.

### ARTICLE INFO

#### Article history:

Received 18 April 2014

Received in revised form

10 July 2014

Accepted 12 July 2014

Available online 19 July 2014

#### Keywords:

Coral-like nanostructure

Complex cobalt-based metal oxide

Lithium ion battery

Co-precipitation

Anode material

### ABSTRACT

A novel porous coral-like  $Zn_{0.5}Ni_{0.5}Co_2O_4$  (ZNCO) is prepared by a facile co-precipitation method using oxalic acid as complex agent, and the  $ZnCo_2O_4$  (ZCO) nanospheres and  $NiCo_2O_4$  (NCO) nanoflakes are also prepared for comparison. The obtained products are systematically characterized by powder X-ray diffraction (XRD), field emission scanning electron microscopy (FESEM), transmission electron microscopy (TEM), and X-ray photoelectron spectroscopy (XPS). The results demonstrate that the controlled metallic elements doping has significant effects on the nanostructure and electrochemical performance of the samples. Compared with the ZCO nanospheres and NCO nanoflakes, the coral-like ZNCO materials with enough free space as anodes in lithium ion batteries (LIBs) exhibit a high initial coulombic efficiency of 84%, a high specific capacity of  $\sim 1445 \text{ mAh g}^{-1}$  at a current rate of  $100 \text{ mA g}^{-1}$  after 50 cycles, and  $\sim 730 \text{ mAh g}^{-1}$  at a current rate of  $1500 \text{ mA g}^{-1}$  after 200 cycles, as well as an excellent rate capability at elevated current rates, such as,  $\sim 1080$  and  $\sim 425 \text{ mAh g}^{-1}$  at current rates of  $500$  and  $6000 \text{ mA g}^{-1}$ , respectively. This work presents a meaningful way for the preparation of mixed metal oxides with porous nanostructure as superior anodes for lithium ion batteries.

© 2014 Elsevier B.V. All rights reserved.

### 1. Introduction

Electrochemical energy storage devices with renewable energy sources are anticipated to deal with the growing energy crisis and various environmental problems. In recent years, Lithium ion batteries (LIBs) have been gradually used as the power sources for electric vehicles and portable electronic devices [1]. It is well known that the vast majority of commercial anode materials used

for LIBs are graphite. However, graphite or modified graphite exhibits a low theoretical specific capacity ( $372 \text{ mAh g}^{-1}$ ) and poor rate capability due to the formation of  $\text{LiC}_6$  in the Li intercalation process [2]. With the increasing demand for higher energy densities LIBs, it is essential to find electrodes with high theoretical specific capacity, excellent cycling performance, and good rate capability.

Nanostructured binary transition metal oxides, such as  $\text{Fe}_3\text{O}_4$  [3],  $\text{CuO}$  [4],  $\text{ZnO}$  [5],  $\text{CoO}$  [6],  $\text{Co}_3\text{O}_4$  [7–10],  $\text{SnO}_2$  [11,12],  $\text{MnO}_2$  [13,14], have been widely investigated as alternative anode materials for LIBs because of their high theoretical specific capacity ( $500$ – $1000 \text{ mAh g}^{-1}$ ), high specific surface area and a short path length for  $\text{Li}^+$  diffusion in comparison with their bulk counterparts [10,14]. More recently, ternary metal oxides from combination of two

\* Corresponding author. Laboratory of Quantum Engineering and Quantum Materials, School of Physics and Telecommunication Engineering, South China Normal University, Guangzhou 510006, PR China. Tel.: +86 20 39318011.

E-mail address: [rq7702@yeah.net](mailto:rq7702@yeah.net) (Q. Ru).

transition metal oxides, or a transition metal oxide and a post-transition metal oxide, with the spinel cubic structure of  $AB_2O_4$ , such as  $ZnCo_2O_4$  (ZCO, 975 mAh g<sup>-1</sup>) [15,16],  $CuCo_2O_4$  [17,18],  $FeCo_2O_4$  [19,20],  $MgCo_2O_4$  [20],  $NiCo_2O_4$  (NCO, 780 mAh g<sup>-1</sup>) [21,22],  $ZnFe_2O_4$  [23,24],  $CoMn_2O_4$  [25], and  $ZnMn_2O_4$  [26,27] have attracted much attention as anode materials for LIBs due to the complementarities and synergies between the two metallic elements during the process of Li insertion or extraction reactions and the reversible reaction with Li giving rise to high storage capacity [28–30]. For example, NCO possess a much better electronic conductivity, at least two orders of magnitude higher, and higher electrochemical activity and more multiple oxidation states/structures than those of nickel oxides and cobalt oxides [31]. Among these transition metal oxides or complex metal oxides, ternary cobalt-based metal oxides have been considered as an attractive anode in LIBs owing to its superiorities such as improved reversible capacities and enhanced cycling stability. However, the intrinsically low conductivity and habitual aggregation of these binary cobalt-based metal oxides lead to low initial coulombic efficiency and rapid capacity fading, which remarkably limits their practical application [32,33].

Interestingly enough, according to the previous researches, the approaches of metallic elements doping and conductive carbon coating have been proved to be effective measures to improve the electric conductivity and the initial coulombic efficiency. As a result, the ternary metal oxides/carbon composites and the mixed metal oxides were studied extensively, such as  $CoFe_2O_4/CNTs$  [33], ZCO/carbon cloth [34], NCO/graphene [22],  $ZnFe_2O_4/C$  [35,36],  $CoFe_2O_4/C$  [32,37,38],  $Mn_{0.5}Co_{0.5}Fe_2O_4$  [29],  $Zn_{1-x}Mn_xFe_2O_4$  [39]. Nevertheless, to the best of our knowledge, as one of the mixed metal oxides,  $Zn_{0.5}Ni_{0.5}Co_2O_4$  with various morphologies are rarely reported as anode materials for LIBs.

Herein, a novel porous coral-like  $Zn_{0.5}Ni_{0.5}Co_2O_4$  (ZNCO, 824 mAh g<sup>-1</sup>) was obtained by a typical co-precipitation method. Compared with other common synthesis methods, such as hydro-thermal method, electrospinning method and high temperature solid state method, the co-precipitation method is more suitable for industrial production due to its low-cost, environment-friendly experiment conditions and high yield (~90%). Meanwhile, the electrodes of the mesoporous ZCO nanospheres and the porous NCO nanoflakes were synthesized by the same method under the same experimental conditions in order to compare with the ZNCO electrodes. As a result, the porous coral-like ZNCO shows higher reversible capacity, better rate performance and higher initial coulombic efficiency compared with the other two electrodes when used as anode materials for LIBs. This work would be meaningful in the preparation of complex oxides with porous nanostructure as anodes for LIBs.

## 2. Experimental

### 2.1. Preparation of the electrode materials

The coral-like ZNCO with porous nanostructure was synthesized by a typical co-precipitation method using hydrated cobalt chloride ( $CoCl_2 \cdot 6H_2O$ , Aladdin, 99.9%), zinc chloride ( $ZnCl_2 \cdot 6H_2O$ , Aladdin, 99.9%) and nickel chloride ( $NiCl_2 \cdot 6H_2O$ , Aladdin, 99.9%) as raw materials, the deionized water (DI) and ethylene glycol (EG) ( $C_2H_6O_2$ , Aladdin, 99.0%) as solvent, and the oxalic acid ( $C_2H_2O_4$ , Aladdin, 99.9%) as complex agent. In a typical synthesis, 12 mmol of  $C_2H_2O_4$  was dissolved in a mixture solution containing 20 mL DI and 40 mL EG with constant stirring at 80 °C for 10 min. Then 30 mL of a mixture solution containing 0.2 M  $CoCl_2 \cdot 6H_2O$ , 0.05 M  $ZnCl_2 \cdot 6H_2O$  and 0.05 M  $NiCl_2 \cdot 6H_2O$  was dropped into the above solution and the pH was adjusted to 7 by adding ammonium hydroxide ( $NH_3 \cdot H_2O$ , Aladdin, 25%) under continuous stirring. The

resultant mixture turned into a turbid suspension and a pale pink precipitate after stirred for 1 h at 80 °C. The precipitate was collected by centrifugation, washed by DI for several times and dried at 120 °C for 10 h in an electric oven followed by natural cooling. Finally, the as-synthesized precursor was further calcined at 450 °C with a temperature rate of 2 °C min<sup>-1</sup> and kept at the same temperature for 4 h in air to get the final products.

Meanwhile, a controlled experiment was also carried to synthesize the porous electrode materials of ZCO and NCO at the same experimental conditions, which was employed for the comparison in the electrochemical measurement.

### 2.2. Material characteristics and electrochemical characteristics testing

The crystal structure and morphology of as-prepared products were characterized by powder X-ray diffraction (XRD; PANalytical X'Pert PRO, Cu/Ka radiation,  $\lambda = 1.5418 \text{ \AA}$ ) and field emission scanning electron microscopy (FESEM; ZEISS ULTRA 55). The chemical components of the products were measured with an energy dispersive X-ray spectrometer (EDS). The microstructures of the as-prepared products were observed by transmission electron microscopy (TEM; JEM-2100HR). Surface analyses of samples were carried out with X-ray photoelectron spectroscopy (XPS, ESCALAB 250 with 150 W Al Ka probe beam). All binding energies were referenced to the C 1s peak (284.6 eV). The specific Brunauer–Emmett–Teller (BET) surface area was determined by  $N_2$  adsorption/desorption on a Coulter SA 3100 surface area analyzer. Thermogravimetric (TG) curves of the precursors were carried out on a Perkin–Elmer TGA 7.

The electrochemical performance was measured using CR2430 button cells. The working electrode was made by mixing 80 wt.% as-prepared material, 10 wt.% Super P as conducting agent, 10 wt.% polyvinylidene fluoride (PVDF) as binder and *N*-methyl-2-pyrrolidone (NMP) as solvent. The electrode slurry was well dispersed via related techniques and spread onto copper foils (10  $\mu\text{m}$ ). After drying in vacuum at 80 °C for 12 h, the electrodes were pressed and punched. The average mass loading of the electrodes was approximately 2.25 mg. And the electrode density was calculated to  $8.85 \times 10^{-4} \text{ g cm}^{-2}$ . CR2430 button cells were assembled in an argon-filled glove box using 1 M LiPF<sub>6</sub> in a mixture of EC/DEC/EMC (1:1:1 by volume, provided by Chei Industries Inc., South Korea) as the electrolyte, Celgard-2400 as the separator and metallic lithium foil as the counter and reference electrode. The galvanostatic discharge-charge performance and the rate performance were tested by LAND CT2001A batteries testing system. The cyclic voltammetry (CV) was carried out on Solartron 1470E electrochemistry system.

## 3. Results and discussion

### 3.1. Phase composition and microstructures

The composition and phase purity of the as-prepared products were first examined by XRD. Fig. 1(a) shows the powder XRD patterns of the coral-like ZNCO, ZCO nanospheres and NCO nanoflakes. It can be seen that all diffraction peaks of the ZCO nanospheres observed from XRD are well consistent with the standard values of the spinel ZCO with cubic structure (JCPDS Card No. 23-1390). The observed diffraction peaks at  $2\theta$  values of 18.9°, 31.2°, 36.8°, 38.5°, 44.8°, 55.6°, 59.3°, and 65.2° correspond to the lattice planes of (111), (220), (311), (222), (400), (422), (511), and (440), respectively. And the resembling XRD patterns are also observed in ZNCO and NCO, which reveals that the ZNCO, ZCO and NCO are of the same cubic spinel structure. It can be seen from the inset pattern which

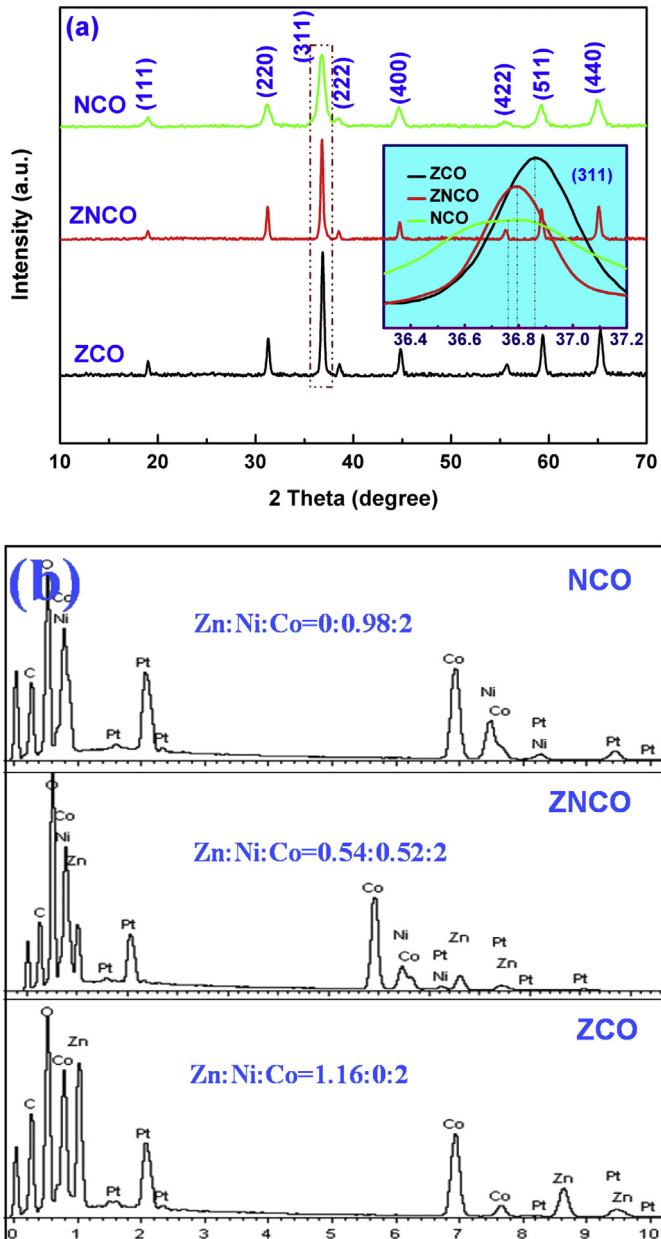


Fig. 1. (a) XRD diffraction patterns of as-prepared ZCO, ZNCO, and NCO, respectively. (b) EDS microanalysis of selected ZCO, ZNCO, and NCO nanoparticles, respectively. The inset of (a) shows the partial enlarged pattern of (311) lattice plane.

shows the partial enlarged view of (311) lattice planes of NCO, ZNCO and ZCO that the  $2\theta$  values of diffraction peaks are about  $36.76^\circ$ ,  $36.80^\circ$  and  $36.86^\circ$ , respectively. Obviously, the diffraction peak of ZNCO is located between NCO and ZCO, which is consistent with the theoretical basis. The lattice parameter values ( $a = b = c$ ) of the coral-like ZNCO, ZCO nanospheres and NCO nanoflakes are  $8.107\text{ \AA}$ ,  $8.099\text{ \AA}$  and  $8.113\text{ \AA}$ , respectively. And the values are approximate to the reported values of ZCO ( $8.095\text{ \AA}$ ) and NCO ( $8.110\text{ \AA}$ ). No other detectable peaks from impurities are observed in the spectrum, which indicates that the as-synthesized products are not the compounds of zinc oxide, nickel oxide or cobalt oxide. The average crystallite sizes of ZNCO, ZCO and NCO are  $\sim 22.9\text{ nm}$ ,  $\sim 21\text{ nm}$  and  $\sim 25.3\text{ nm}$ , which are calculated by Scherrer equation using all diffraction peaks among the XRD patterns. Additionally, in order to quantify the atomic ratio of Zn, Ni and Co, the as-prepared

ZNCO, ZCO and NCO were further analyzed by EDS. As shown in Fig. 1(b), the elements of Zn, Ni, Co, O can be seen clearly and the atomic ratios of Zn, Ni, Co exhibited in the EDS patterns are close to the presumed stoichiometric ratios.

The XPS was carried out to obtain further information about the phase purity, chemical composition and the chemical bonding state of as-prepared ZNCO, as shown in Fig. 2. All of the binding energies obtained in the XPS analysis were corrected for specimen charging by referencing the C 1s peak to 284.6 eV. Fig. 2(a) shows a typical survey XPS spectrum and indicates the presence of Zn, Co, Ni and O, as well as C from the reference, and the absence of other impurities. Fig. 2(b) depicts a high-resolution XPS spectrum of Co 2p, where two spin-orbit lines centered at 779.7 eV and 794.7 eV can be ascribed to Co 2p<sub>3/2</sub> and Co 2p<sub>1/2</sub> orbits, respectively [40–42]. There are also two shakeup satellites (identified as "Sat."). After refined fitting, the spectrum can be mainly deconvoluted into four peaks. Among them, the two peaks at 779.6 eV and 794.6 eV can be attributed to the existence of Co<sup>3+</sup>, while the other two peaks at 781.1 eV and 795.9 eV are characteristic of Co<sup>2+</sup>. The Zn 2p high-resolution spectrum (Fig. 2(c)) consists of two major peaks located at 1020.6 eV and 1043.7 eV, which are assigned to Zn<sup>2+</sup> with Zn 2p<sub>3/2</sub> and Zn 2p<sub>1/2</sub> orbits, respectively [43]. It is similar to the Co 2p spectrum. The spectrum of Ni 2p consists of two spin-orbit doublets at 855.2 eV and 872.4 eV characteristic of Ni<sup>2+</sup> and Ni<sup>3+</sup> and two shakeup satellites (Fig. 2(d)) [40]. Therefore, it is reasonable to conclude that the elements of Zn, Co and Ni present as the form of Zn<sup>2+</sup>, Co<sup>2+</sup>, Co<sup>3+</sup>, Ni<sup>2+</sup> and Ni<sup>3+</sup> in the coral-like ZNCO nanospheres. In addition, the Zn, Ni and Co atomic ratio of the ZNCO nanospheres calculated by the area of deconvoluted peaks is about 0.58 : 0.53 : 2, which is well consistent with the EDS analysis result and the presumed stoichiometry.

The ZCO nanospheres, coral-like ZNCO and NCO nanoflakes were prepared by co-precipitation method followed by calcinations. The morphologies of the obtained samples were investigated by SEM. Fig. 3a & b show the different magnification SEM images of the as-synthesized ZCO. It can be seen from Fig. 3(a) that the ZCO products are composed of nanospheres with a diameter of 0.5–1.5  $\mu\text{m}$ . A presentative individual nanosphere selected from Fig. 3(a) (in the web version) (marked with red box) is shown in higher-magnification Fig. 3(b), where the nanosphere with mesoporous nanostructure is actually composed of nanoparticles with an average size of 10–30 nm. Fig. 3(c & d) show the different magnification SEM images of the as-synthesized ZNCO. The ZNCO presents a porous coral-like nanostructure (Fig. 3(c)). In order to obtain further information about the morphologies and microstructures of ZNCO, Fig. 3(d) shows the higher-magnification SEM of selected region. Obviously, the porous coral-like nanostructure is made up of a series of dendrite-like ZNCO which is connected by nanoparticles with a mean size of 10–30 nm. In Fig. 3(e & f), the NCO shows a porous architecture with NCO nanoflakes stood together freely. Carefully, we can find that the NCO nanoflakes with a thickness of 30–80 nm are composed of uniform NCO nanocrystals with an average diameter of 10–30 nm, and many nanopores are shown in the NCO nanoflakes, which maybe ascribe to the decomposition of NCO precursor to NCO. Herein, the same process was adopted to prepare the above three electrodes with different morphologies, which maybe majorly ascribed to the large differences of metallic atom ratio among the three electrodes. Moreover, several previous papers also gave the same results that the measures of stoichiometric ratio modification and metallic elements doping have effects on the morphologies of the as-prepared products in the same process [44–46].

In addition, the specific surface area of ZCO nanospheres, coral-like ZNCO and NCO nanoflakes measured by the Brunauer–Emmett–Teller (BET) method is  $22.9$ ,  $34.8$ ,  $51.0\text{ m}^2\text{ g}^{-1}$ ,

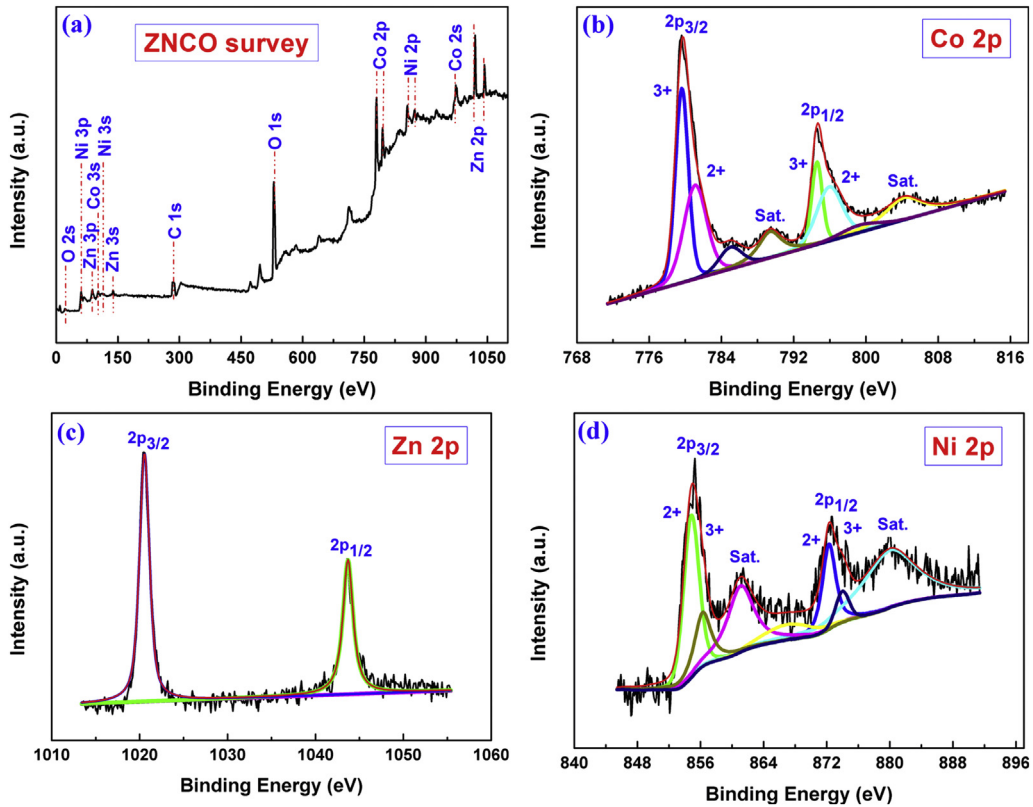
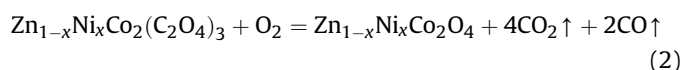
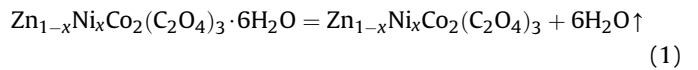


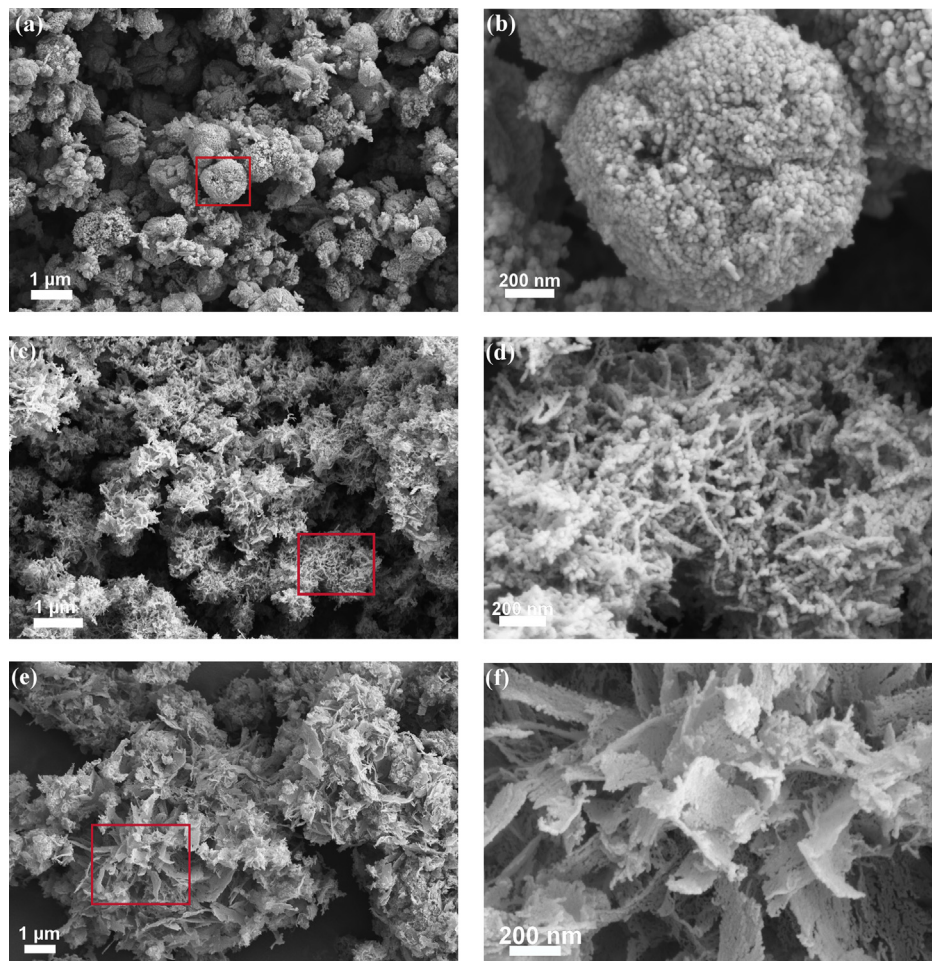
Fig. 2. XPS spectra for the coral-like ZNCO: (a) survey spectrum, (b) Co 2p, (c) Zn 2p, (d) Ni 2p.

respectively. Therefore, according to the SEM images and the BET values of ZCO nanospheres, coral-like ZNCO and NCO nanoflakes, it is reasonable to conclude that the specific surface area, free space and pore size of the as-prepared products rise apparently with the doping of element Ni. Moreover, the architecture of as-prepared products tends to randomness. The electrode materials with high specific surface area and adequate free spaces are conducive to the alleviation of volume changes and the rapid transmission of Li<sup>+</sup> during Li insertion and extraction which are important to the excellent electrochemical performance.

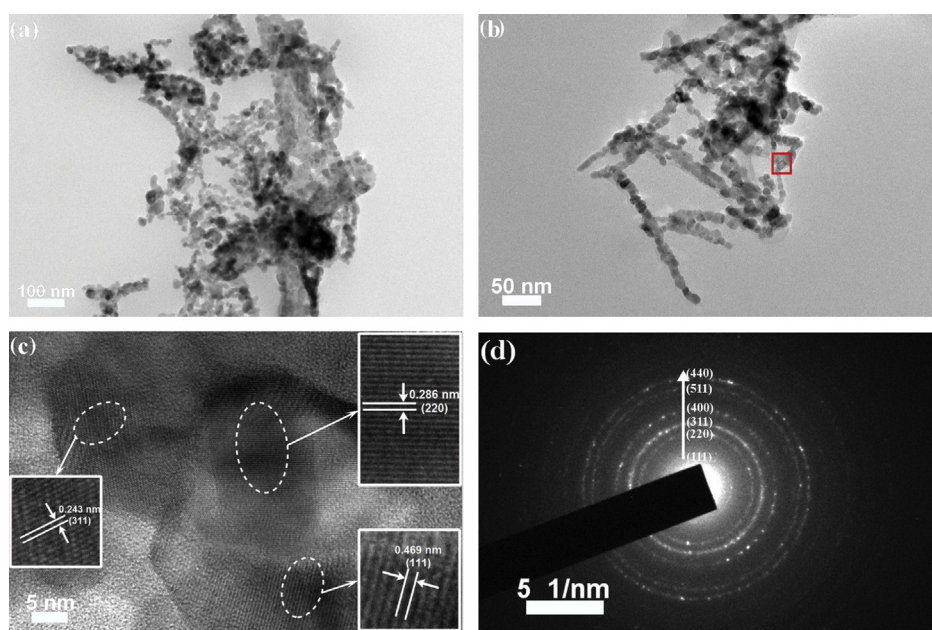
TEM was used to further investigate the detailed microstructure of the synthesized ZNCO material. Fig. 4(a & b) further confirm the porous coral-like nanostructure of the as-prepared ZNCO, which is composed of nanoparticles with a diameter of 10–30 nm. And the result is similar to the above SEM observation. A presentative high-resolution TEM (HRTEM) image selected from the marked area (Fig. 4(b)) is shown in Fig. 4(c), which further demonstrates the high crystallinity of as-prepared ZNCO for its distinct lattice fringes. The insert pictures of Fig. 4(c) show the magnification images of the selected regions (marked with white cycles) in Fig. 4(c). The distance between adjacent lattice fringes is measured at about 2.43 Å, 4.69 Å and 2.86 Å, which is close to the reported d-values between the (311) planes, (111) planes and (220) planes of spinel cubic ZCO or NCO. Therefore, it is reasonable to deduce, combining with the analysis of the XRD spectrum, that the lattice fringes mentioned above correspond to the (311) planes, (111) planes and (220) planes of as-prepared spinel cubic ZNCO. The crystal structural of ZNCO products was further determined according to the selected area electron diffraction (SAED) pattern shown in Fig. 4(d), indicating a polycrystalline nature for the coral-like ZNCO, and all the diffraction rings can be indexed as (111), (220), (311), (400), (511) and (440) from the inside out, respectively.

Fig. 5 shows the thermal property of all the precursors characterized by thermogravimetric (TG) technique from room temperature to 600 °C at a heating rate of 5 °C min<sup>-1</sup> in flowing air atmosphere. It can be seen clearly that all the TG curves exhibit two distinct weight loss steps. The first ~20% weight loss between 100 and 180 °C can be attributed to the evaporation of moisture and the decomposition of crystal water in the precursors, while the slight weight loss between 180 and 260 °C in the TG curves maybe ascribed to the decomposition of a small amount of organic species adsorbed on the surfaces of the precursors. The following ~40% weight loss occurs at 260–340 °C, which is assigned to the conversion of anhydrous precursors to spinel cubic crystals. It is obvious that the decomposition temperature of ZCO nanospheres is higher than the precursors of coral-like ZNCO and NCO nanoflakes, which is possibly owing to the different nanostructures of the precursors. There is almost no weight loss between 340 and 600 °C in the TG curves and the final residue of spinel cubic crystals is about ~40%. Furthermore, the final residual mass of ZCO, ZNCO and NCO decreases slightly for the difference between the relative molecular mass of Zn and Ni. Therefore, it can be concluded that the thermal temperature (450 °C) is enough to remove the complex agent among the precursors completely and obtain crystals with high crystallinity. The values of two weight loss steps mentioned above are well consistent with the theoretical values. The decomposition of Zn<sub>1-x</sub>Ni<sub>x</sub>Co<sub>2</sub>(C<sub>2</sub>O<sub>4</sub>)<sub>3</sub>·6H<sub>2</sub>O (0 ≤ x ≤ 1) can be expressed as the following reactions [44]:





**Fig. 3.** Typical SEM profiles of ZCO nanospheres (a & b), coral-like ZNCO (c & d), and NCO nanoflakes (e & f), respectively.



**Fig. 4.** TEM images of the coral-like ZNCO: (a & b) full size, (c) HRTEM, (d) SAED, the insert pictures is partial enlarged view of (c).

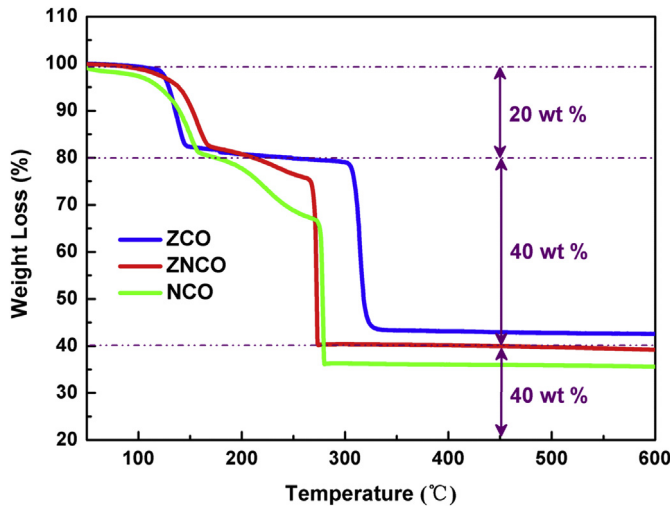


Fig. 5. TG curves for the as-prepared ZCO, ZNCO, and NCO precursors, respectively.

### 3.2. Electrochemical analysis

To survey the applicability of the as-prepared samples as anode materials for LIBs, the electrochemical performance of the anode materials was investigated. The galvanostatic discharge-charge profiles for the first two cycles at a current density of  $100 \text{ mA g}^{-1}$  in the voltage range of  $0.01$ – $3.0 \text{ V}$  are exhibited in Fig. 6(a). It can be seen that the discharge–charge curves of ZCO, ZNCO and NCO present the similar shape. The first discharge curves exhibit a long voltage plateau at  $1.0$ – $0.9 \text{ V}$ , followed by sloping down to the cutoff voltage of  $0.01 \text{ V}$ , while the 2nd discharge cycles produce a sloping

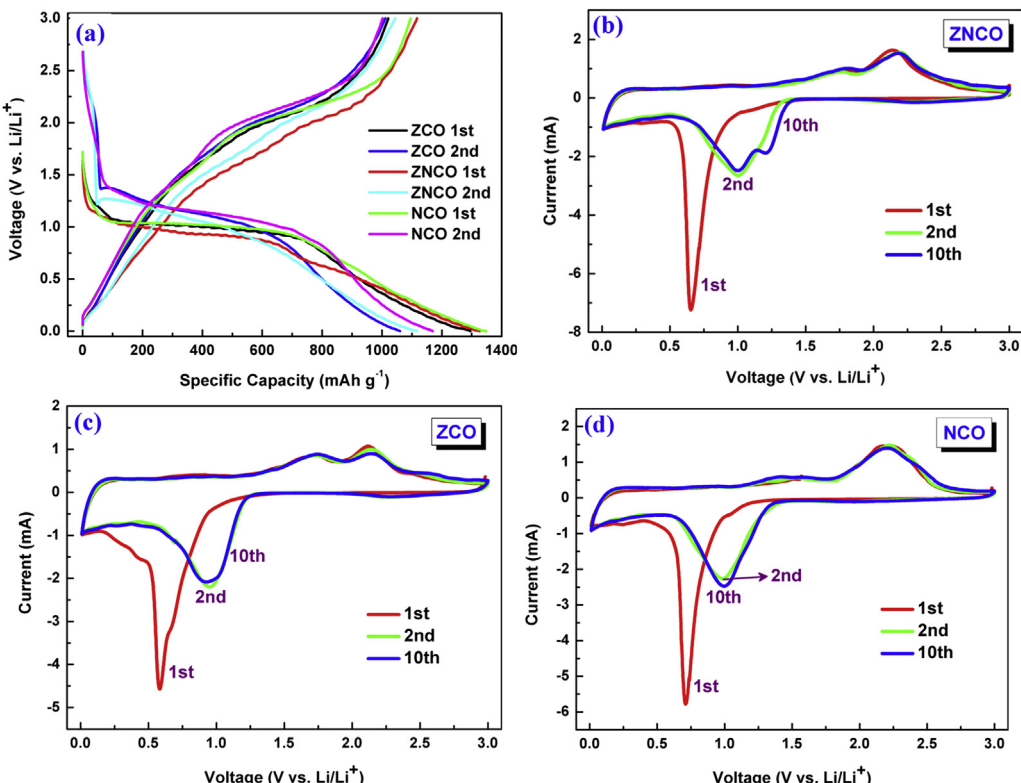


Fig. 6. (a) Discharge–charge profiles of as-prepared ZCO, ZNCO, and NCO electrodes in the 1st and 2nd cycles at a constant current of  $100 \text{ mA g}^{-1}$ , respectively. CV profiles of as-prepared ZNCO (b), ZCO (c), and NCO (d) electrodes in the 1st, 2nd, and 10th cycles at a scan rate of  $0.1 \text{ mV s}^{-1}$  between  $0.01$  and  $3.0 \text{ V}$ , respectively.

potential plateau beginning at  $\sim 1.35 \text{ V}$  which is higher than the 1st cycles and the gradient of discharge plateau becomes steeper. At the same time, it can be seen that the discharge-charge voltage plateaus are well consistent with the peaks in the CV curves as shown in Fig. 6(b–d). The initial discharge specific capacities are  $\sim 1295 \text{ mAh g}^{-1}$  for ZCO,  $\sim 1326 \text{ mAh g}^{-1}$  for ZNCO and  $\sim 1348 \text{ mAh g}^{-1}$  for NCO, corresponding to initial coulombic efficiencies of about 79%, 84% and 81%, respectively. It has been proved that the initial capacity loss is related to the formation of a solid electrolyte interphase (SEI) film on the surface of active materials [34,47], the reduction of metal oxide to metal with  $\text{Li}_2\text{O}$  formation [44], and the decomposition of electrolyte. Meanwhile, all the first discharge capacities are much higher than the theoretical capacity ( $900$ – $1000 \text{ mAh g}^{-1}$ ), which may be ascribed to the formation of SEI film and organic polymeric/gel-like layer by electrolyte decomposition [48,49]. Furthermore, the interfacial storage originated from the obtained porous structures is considered to be responsible for the high extra capacity [18,50]. In conclusion, the initial specific capacity and the initial coulombic efficiency of the as-prepared ZNCO electrodes present a higher value compared with the electrodes of ZCO and NCO owing to the complementarities and synergies among different metallic elements in the Li discharge-charge process, which means that ZNCO electrodes possess a much better electronic conductivity and higher electrochemical activity than those of  $\text{ZnO}$ ,  $\text{NiO}$  and  $\text{Co}_3\text{O}_4$  owing to the relatively low activation energy for electron transfer between cations, and ZNCO is expected to offer richer redox reactions than the three corresponding single component oxides [30,31,51,52].

Fig. 6(b–d) show the 1st, 2nd, and 10th CV curves of the ZNCO, ZCO and NCO electrodes at a scan rate of  $0.1 \text{ mV s}^{-1}$  in the potential range of  $0.01$ – $3.0 \text{ V}$  versus  $\text{Li}/\text{Li}^+$ , respectively. During the first cycle, for the CV curves of ZNCO shown in Fig. 6(b), there is a reduction peak observed at  $\sim 0.6 \text{ V}$ , which is substantially different

from the followed cycles onwards. The reduction peak at  $\sim 0.6$  V can be attributed to the reduction of ZNCO to Zn, Ni and Co, and the formation of  $\text{Li}_2\text{O}$  corresponding to the electrochemical Li insertion reaction of Eq. (3). The reduction peak at  $<0.4$  V corresponding to the formation of  $\text{LiZn}$  for Zn react with Li can be barely seen. While, in the first cycle of ZCO shown in Fig. 6(c), there exists a measurable reduction peak at  $<0.4$  V compared with the first cycle CV of ZNCO, which is owing to the electrochemical Li insertion reaction of Eq. (4). Two oxidation peaks can be ascribed to the removal of Li and the formation of  $\text{NiO}$  at  $\sim 1.6$  V,  $\text{ZnO}$  at  $\sim 1.8$  V and  $\text{Co}_3\text{O}_4$  at  $\sim 2.1$  V [18,53,54], corresponding to the electrochemical Li extraction reactions of Eqs. (5)–(8). The peaks at  $\sim 1.6$  V and at  $\sim 1.8$  V are almost merged into one flat peak for the closeness between them. In the 2nd and 10th cycles, the reduction peak at  $\sim 0.6$  V in the 1st cycle moves to  $\sim 1.0$  V due to less or no formation of SEI film and irreversible reduction reaction [55,56], while the two oxidation peaks are almost no shift and overlap very well from 1st to 10th. Furthermore, the CV curves of the subsequent cycles after the first cycle overlap very well, indicating good electrochemical reversibility in the Li insertion and extraction reactions, and the stability of the assembled structure. As to the CV curves of ZCO and NCO shown in Fig. 6(c and d), compared with the CV curves of ZNCO, the reduction peaks in the first cycle drift slightly ( $\sim 0.1$  V), respectively. However, with the doping of Ni, the oxidation peaks at  $\sim 1.6$  V become more and more apparent while the peaks at  $\sim 1.8$  V disappear slowly. According to the previous researches of ZCO and NCO [19,48,55–57], the discharge and charge processes are believed to proceed as follows:

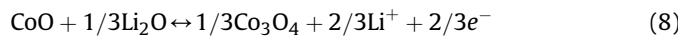
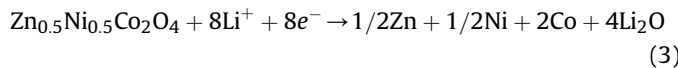


Fig. 7(a) shows the cycling performance and the coulombic efficiency of ZCO nanospheres, coral-like ZNCO and NCO nanoflakes at a current density of  $100 \text{ mA g}^{-1}$ . For the initial 20 cycles except the 1st cycle, it can be observed that the reversible capacities of all the electrodes are gradually increasing. This phenomenon may be ascribed to the formation of a polymeric surface film attached to the active material [55,58,59]. The similar issue is also mentioned in previous papers and all of them offer the same explanations [34,55,60]. After 50 cycles, coral-like ZNCO demonstrates the highest reversible discharge capacity of  $\sim 1445 \text{ mAh g}^{-1}$  as compared to ZCO nanospheres with discharge capacity of  $\sim 1426 \text{ mAh g}^{-1}$  and NCO nanoflakes with discharge capacity of  $\sim 451 \text{ mAh g}^{-1}$ . Meanwhile, Fig. 7(a) presents the coulombic efficiencies in the processes of discharge–charge. The initial coulombic efficiency of the coral-like ZNCO is 84.2%, and it can achieve as high as 97% from 5th to 50th cycle, which demonstrates the good electrochemical performance once again. These results prove that the appropriate doping of element Ni in the ZCO electrodes substantially enhance the capacity and cycling properties of the electrodes. In conclusion, the coral-like ZNCO electrodes with good reversible capacity and cycling stability can be explained by the reason that

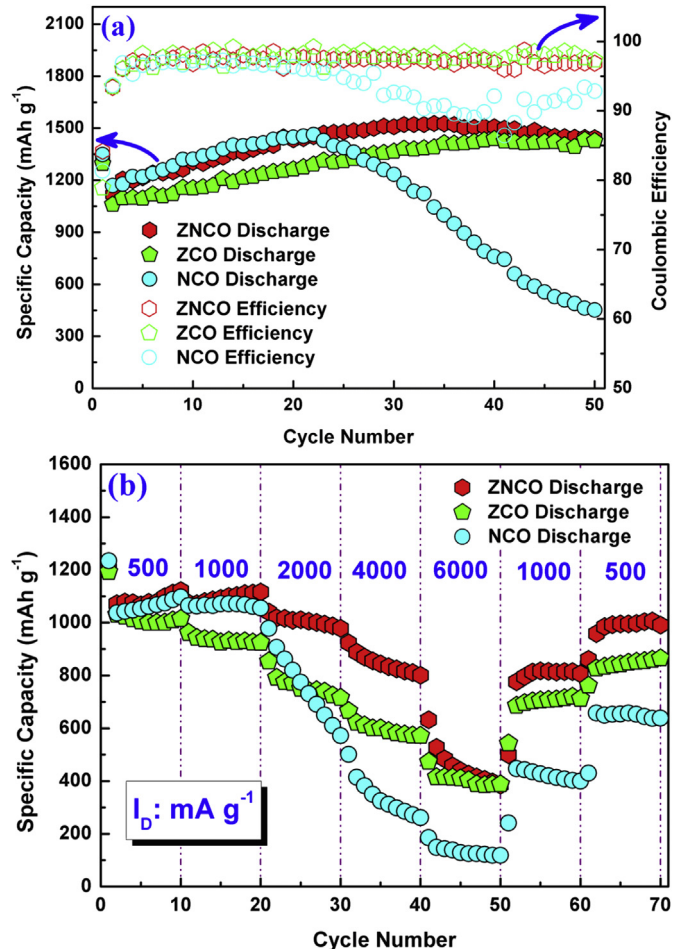
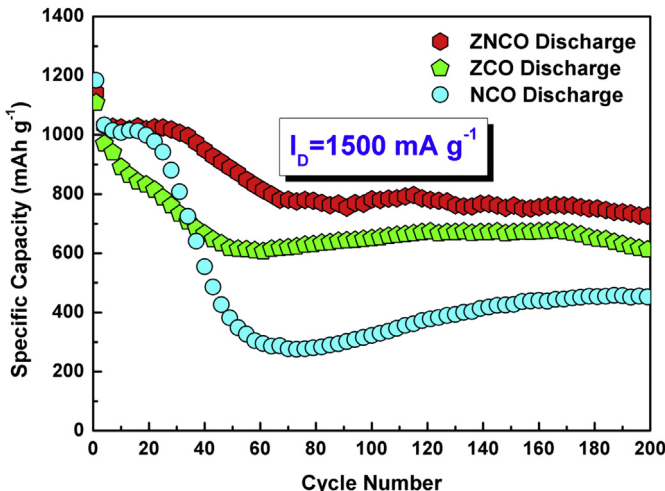


Fig. 7. (a) Cycling performance of as-prepared ZCO, ZNCO, and NCO electrodes for the first 50 cycles and the corresponding coulombic efficiency at a constant current of  $100 \text{ mA g}^{-1}$ , respectively. (b) Rate performance of as-prepared ZCO, ZNCO, and NCO electrodes at current densities of 500, 1000, 2000, 4000, and  $6000 \text{ mA g}^{-1}$ , respectively.

the porous coral-like nanostructure built up by dendrite-like ZNCO has high specific surface area and sufficient free-spaces, and that the ZNCO particles used to compose the dendrite-like ZNCO are nanosize [61,62]. In addition, the complementarities and synergies between different metallic elements in the Li discharge–charge process are also beneficial to the excellent electrochemical performance [30]. Moreover, the element Ni doping can be helpful to alleviate volume expansion during the processes of charge–discharge.

To further confirm the good performance of as-prepared coral-like ZNCO, the rate capability of the ZCO, ZNCO and NCO at different current densities ranging from 500 to  $6000 \text{ mA g}^{-1}$  is shown in Fig. 7(b). The specific capacity decreases from  $\sim 1010$  to  $\sim 410 \text{ mAh g}^{-1}$  for ZCO, from  $\sim 1080$  to  $\sim 425 \text{ mAh g}^{-1}$  for ZNCO and from  $\sim 1060$  to  $\sim 110 \text{ mAh g}^{-1}$  for NCO when the current density increases from 500 to  $6000 \text{ mA g}^{-1}$ , respectively. The specific capacity of coral-like ZNCO rebounds to  $\sim 985 \text{ mAh g}^{-1}$  when the current density is back to  $500 \text{ mA g}^{-1}$  after 70 cycles of discharge–charge, and it is almost equal to the capacity of the initial ten cycles at the current density of  $500 \text{ mA g}^{-1}$ . While the capacities of ZCO and NCO can only rebound to  $\sim 830$  and  $\sim 640 \text{ mAh g}^{-1}$ , respectively. Therefore, it can be concluded that the controllable doping of Ni content can conduce to a better rate performance.



**Fig. 8.** Cycling performance of as-prepared ZCO, ZNCO, and NCO electrodes for 200 cycles at a large current of  $1500 \text{ mA g}^{-1}$ , respectively.

In order to investigate the long cycling performance at a large current density, Fig. 8 shows the cycling performance of as-prepared products at a large current density of  $1500 \text{ mA g}^{-1}$  for 200 cycles. It can be observed that the reversible capacities of all the electrodes exhibit an obvious decreasing tendency during 30–60

cycles. Interestingly, the electrode of coral-like ZNCO nicely yields a discharge capacity of  $\sim 730 \text{ mAh g}^{-1}$  after 200 cycles, while the electrodes of ZCO nanospheres and NCO nanoflakes just retain at  $\sim 615$  and  $\sim 450 \text{ mAh g}^{-1}$  by the 200th cycle, respectively. The retained reversible capacity of coral-like ZNCO is almost two times higher than the capacity of  $372 \text{ mAh g}^{-1}$  given by commercial graphite. The reasons for the obvious capacities decrease maybe as follows [22,63–65]: (1) the continuous loss of active materials due to the embedding of metallic cobalt, zinc and nickel in  $\text{Li}_2\text{O}$  matrix partially, especially it occurs at a high rate; (2) the aggregation of the active species to large clusters cannot be fully eliminated; (3) the structure strain of the electrode material is unavoidable during cycling even though the sufficient free space of porous nanostructure may accommodates the volume variations of the active materials, which leads to a portion of active materials failure.

The SEM images of the electrodes (Fig. 9) after 200 discharge–charge cycles were employed to further explain the excellent electrochemical behavior of the coral-like ZNCO. All the cracks in SEM images can be attributed to the repeated volume change by conversion reaction between metal oxides and metals. It can be observed from Fig. 9(a and b) that the texture of the ZCO nanospheres (marked with white cycles) can be well retained, and the surface of the electrode is smooth except some nanocracks (marked with white arrows) for the formation of SEI film. The morphology of the coral-like ZNCO obtained by using element Ni to substitute partially element Zn in ZCO nanospheres is shown in Fig. 9(c and d). Obviously, some narrow cracks and many nanopores

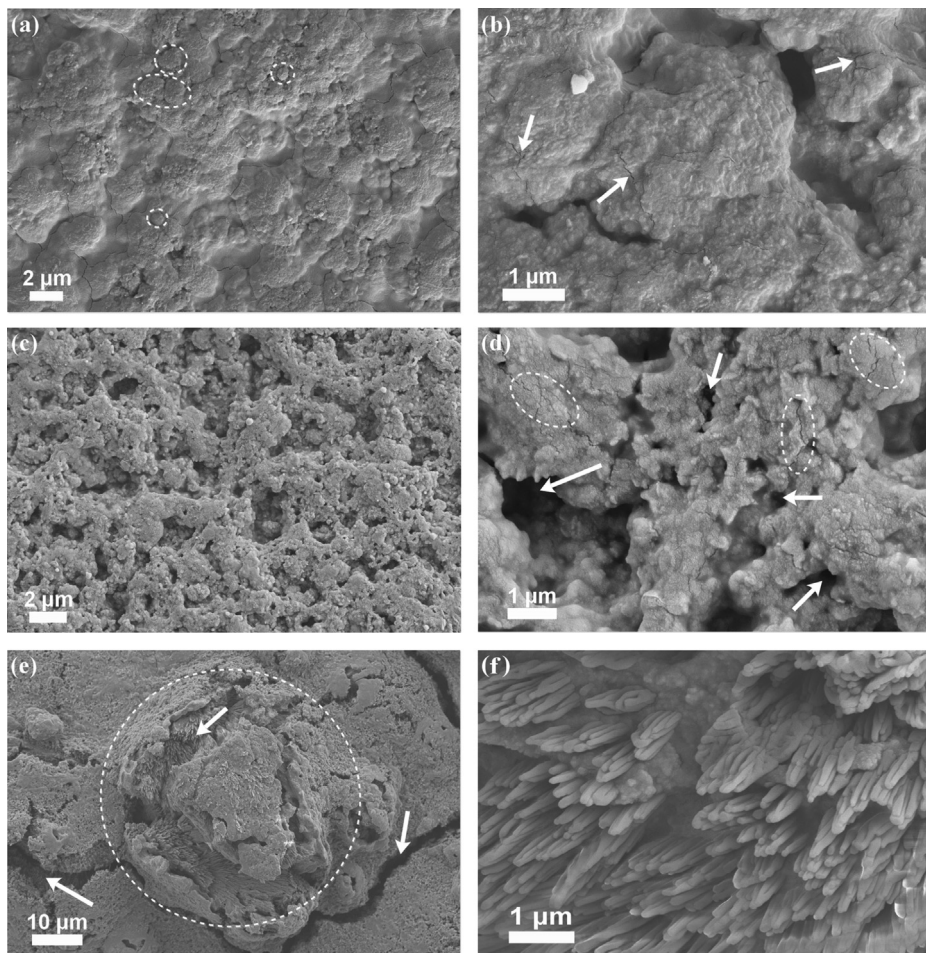


**Fig. 9.** Typical SEM images of ZCO nanospheres (a & b), coral-like ZNCO (c & d), and NCO nanoflakes (e & f) electrodes after 200 cycles at a current of  $1500 \text{ mA g}^{-1}$ , respectively.

(marked with white cycles and arrows) present on the surface of the electrode due to a slight volume change caused by the doping of Ni. However, on the one hand, these narrow cracks and nanopores will not lead to the detachment of the anode materials from the current collector and the failure of the active materials. On the other hand, they not only offer a short pathway for  $\text{Li}^+$  diffusion, but also increase the opportunities for the contact between  $\text{Li}^+$  and active materials. While, such as the morphology of the NCO electrode shown in Fig. 9(e and f), a large clusters of dendritic crystals (marked with white cycles) emerging on the surface of the electrode lead to the pulverization of electrodes and the detachment of active materials from the current collector. So, a certain amount of element Ni doping could improve the electrochemical performance to a great extent.

#### 4. Conclusions

In summary, a simple typical co-precipitation method followed by a thermal annealing procedure in air atmosphere is applied to synthesize the ZCO nanospheres, coral-like ZNCO and NCO nano-flakes with porous nanostructures. The anode materials of coral-like ZNCO with high initial coulombic efficiency, good cyclic ability and excellent rate performance were obtained by substituting the element Zn with element Ni in the spinel binary cobalt-based metal oxides. This research not only proves the metallic elements doping methods could change the morphologies and the electrochemical performance of complexed transition metal oxides with spinel cubic structure, but also reveals the doping content of metallic element is absolutely vital for the battery properties. In addition, the preparation method used in this paper is easy for industrialization due to its inexpensive, environment-friendly experiment conditions and high yield.

#### Acknowledgments

This work was supported by National Natural Science Foundation of China (Grant No. 51101062 and 51171065), Science and Technology Project of Guangzhou City, China (Grant No. 2011J4100075), Foundation for Distinguished Young Talents in Higher Education of Guangdong, China (Grant No. LYM09052), China Scholarship Council (No. 201308440314), Extracurricular Science Foundation for Students in South China Normal University of Guangdong, China (Grant No. 13WDGB03), The Scientific Research Foundation of Graduate School of South China Normal University (Grant No. 2013KYJJ039), The Natural Science Foundation of Guangdong Province (Grant No. S2012020010937, 10351063101000001), and University-Industry Cooperation Projects of Guangdong province, Ministry of Education and Science & Technology (Grant No. 2011A091000014).

#### References

- J.M. Tarascon, M. Armand, *Nature* 414 (2001) 359.
- S. Flandrois, B. Simon, *Carbon* 37 (1999) 165.
- B. Jin, A.H. Liu, G.Y. Liu, Z.Z. Yang, X.B. Zhong, X.Z. Ma, M. Yang, H.Y. Wang, *Electrochim. Acta* 90 (2013) 426.
- M.V. Reddy, C. Yu, J.H. Fan, K.P. Loh, B.V.R. Chowdari, *Appl. Mater. Interfaces* 5 (2013) 4361.
- O.B. Chae, S.J. Park, J.H. Ryu, S.M. Oh, *J. Electrochem. Soc.* 160 (2013) A11.
- Y.M. Sun, X.L. Hu, W. Luo, Y.H. Huang, *J. Mater. Chem.* 22 (2012) 13826.
- G. Chen, E.G. Fu, M. Zhou, Y. Xu, L. Fei, S.G. Deng, V. Chaitanya, Y.Q. Wang, H.M. Luo, *J. Alloys Compd.* 578 (2013) 349.
- X.C. Dong, H. Xu, X.W. Wang, Y.X. Huang, Mary B. Chan-Park, H. Zhang, L.H. Wang, W. Huang, P. Chen, *ACS Nano* 6 (2012) 3206.
- X.Y. Yao, X. Xin, Y.M. Zhang, J. Wang, Z.P. Liu, X.X. Xu, *J. Alloys Compd.* 521 (2012) 95.
- Z. Lin, W. Yue, D. Huang, J. Hu, X. Zhang, Z. Yuan, X. Yang, *RSC Adv.* 2 (2012) 1794.
- Q.H. Tian, Z.X. Zhang, L. Yang, S. Hirano, *J. Power Sources* 253 (2014) 9.
- J.X. Guo, L. Chen, G.J. Wang, X. Zhang, F.F. Li, *J. Power Sources* 246 (2014) 862.
- H. Lai, J.X. Li, Z.G. Chen, Z.G. Huang, *Appl. Mater. Interfaces* 4 (2012) 2325.
- Y. Ren, A.R. Armstrong, F. Jiao, P.G. Bruce, *J. Am. Chem. Soc.* 132 (2010) 996.
- X. Song, Q. Ru, B.B. Zhang, S.J. Hu, B.N. An, *J. Alloys Compd.* 585 (2014) 518.
- L.L. Hu, B.H. Qu, C.C. Li, Y.J. Chen, L. Mei, D.N. Lei, L.B. Chen, Q.H. Li, T.H. Wang, *J. Mater. Chem. A* 1 (2013) 5596.
- S.J. Sun, Z.Y. Wen, J. Jin, Y.M. Cui, Y. Lu, *Microporous Mesoporous Mater.* 169 (2013) 242.
- C. Liang, M.X. Gao, H.G. Pan, Y.F. Liu, M. Yan, *J. Alloys Compd.* 575 (2013) 246.
- Z.L. Zhang, Y.H. Wang, D. Li, Q.Q. Tan, Y.F. Chen, Z.Y. Zhong, F.B. Su, *Ind. Eng. Chem. Res.* 52 (2013) 14906.
- Y. Sharma, N. Sharma, G.V. Subba Rao, B.V.R. Chowdari, *Solid State Ionics* 179 (2008) 587.
- J.F. Li, S.L. Xiong, Y.R. Liu, Z.C. Ju, Y.T. Qian, *Appl. Mater. Interfaces* 5 (2013) 981.
- Y.J. Chen, J. Zhu, B.H. Qu, B.G. Lu, Z. Xu, *Nano Energy* 3 (2014) 88.
- N.N. Wang, H.Y. Xu, L. Chen, X. Gu, J. Yang, Y.T. Qian, *J. Power Sources* 247 (2014) 163.
- F. Mueller, D. Bresser, E. Paillard, M. Winter, S. Passerini, *J. Power Sources* 236 (2013) 87.
- M.H. Kim, Y.J. Hong, Y.C. Kang, *RSC Adv.* 3 (2013) 13110.
- Z.M. Zheng, Y.L. Cheng, X.B. Yan, R.T. Wang, P. Zhang, *J. Mater. Chem. 2* (2014) 149.
- L.F. Xiao, Y.Y. Yang, J. Yin, Q. Li, L.Z. Zhang, *J. Power Sources* 194 (2009) 1089.
- L. Zhou, D. Zhao, X.W. Lou, *Adv. Mater.* 24 (2012) 745.
- Z.L. Zhang, Y.H. Wang, D. Li, Q.Q. Tan, Y.F. Chen, Z.Y. Zhong, F.B. Su, *Ind. Eng. Chem. Res.* 42 (2013) 14906.
- J.F. Li, J.Z. Wang, D. Wexler, D.Q. Shi, J.W. Liang, H.K. Liu, S.Q. Xiong, Y.T. Qian, *J. Mater. Chem. A* 1 (2013) 15292.
- T.Y. Wei, C.H. Chen, H.C. Chien, S.Y. Lu, C.C. Hu, *Adv. Mater.* 22 (2010) 347.
- Z.L. Zhang, Y.H. Wang, M.J. Zhang, Q.Q. Tan, X. Lv, Z.Y. Zhong, F.B. Su, *J. Mater. Chem. A* 1 (2013) 7444.
- H. Huang, Y. Liu, J.L. Wang, M. Gao, X. Peng, Z. Ye, *Nanoscale* 5 (2013) 1785.
- B. Liu, J. Zhang, X. Wang, G. Chen, D. Chen, C. Zhou, G. Shen, *Nano Lett.* 12 (2012) 3005.
- L.M. Yao, X.H. Hou, S.J. Hu, J. Wang, M. Li, C. Su, M.O. Tade, Z.P. Shao, X. Liu, *J. Power Sources* 258 (2014) 305.
- J.H. Sui, C. Zhang, D. Hong, J. Li, Q. Cheng, Z.G. Li, W. Cai, *J. Mater. Chem.* 22 (2012) 13674.
- L.J. Wu, Q.Z. Xiao, Z.H. Li, G.T. Lei, P. Zhang, L. Wang, *Solid State Ionics* 215 (2012) 24.
- S.Y. Liu, J. Xie, C.C. Fang, G.S. Cao, T.J. Zhu, X.B. Zhao, *J. Mater. Chem.* 22 (2012) 19738.
- P.F. Teh, S.S. Pramana, Y. Sharma, Y.W. Ko, S. Madhavi, *Appl. Mater. Interfaces* 5 (2013) 5461.
- J.G. Kim, D.L. Pugnire, D. Battaglia, M.A. Langell, *Appl. Surf. Sci.* 165 (2000) 70.
- J.F. Marco, J.R. Gancedo, M. Gracia, J.L. Guatier, E.I. Rios, H.M. Palmer, C. Greaves, F.J. Berry, *J. Mater. Chem.* 11 (2001) 3087.
- A.L. Rosa-Toro, R. Berenguer, C. Quijada, F. Montilla, E. Morallon, J.L. Vazquez, *J. Phys. Chem. B* 110 (2006) 24021.
- S. Vijayanand, P.A. Joy, H.S. Potdar, D. Patil, P. Patil, *Sens. Actuators B Chem.* 152 (2011) 121.
- D. Deng, J.Y. Lee, *Nanotechnology* 22 (2011) 355401.
- J.F. Li, S.L. Xiong, X.W. Li, Y.T. Qian, *Nanoscale* 5 (2013) 2045.
- Q. Li, L.W. Yin, Z.P. Li, X.K. Wang, Y.X. Qi, J.Y. Ma, *Appl. Mater. Interfaces* 5 (2013) 10975.
- H.W. Liu, J. Wang, *Electrochim. Acta* 92 (2013) 371.
- N. Munichandraiah, L.G. Scanlon, R.A. Marsh, *J. Power Sources* 72 (1998) 203.
- S. Laruelle, S. Gruegeon, P. Poizot, M. Dolle, L. Dupont, J.M. Tarascon, *J. Electrochem. Soc.* 149 (2002) A627.
- P. Balaya, H. Li, L. Kienle, J. Maier, *J. Adv. Funct. Mater.* 13 (2003) 621.
- C.Z. Yuan, H.B. Wu, Y. Xie, X.W. (David) Lou, *Angew. Chem.* 53 (2014) 1488.
- M.V. Reddy, G.V. Subba Rao, B.V.R. Chowdari, *Chem. Rev.* 113 (2013) 5364.
- H.C. Liu, S.K. Yen, *J. Power Sources* 166 (2007) 478.
- C.Q. Zhang, J.P. Tu, Y.F. Yuan, X.H. Huang, X.T. Chen, F. Mao, *J. Electrochem. Soc.* 154 (2007) 65.
- N. Du, Y.F. Xu, H. Zhang, J.X. Yu, C.X. Zhai, D.R. Yang, *Inorg. Chem.* 50 (2011) 3320.
- Y. Sharma, N. Sharma, G.V.S. Rao, B.V.R. Chowdari, *Adv. Funct. Mater.* 17 (2007) 2855.
- X.F. Li, A. Dhanabalan, C.L. Wang, *J. Power Sources* 196 (2011) 9625.
- K.M. Shaju, F. Jiao, A. Debart, P.G. Bruce, *Phys. Chem. Chem. Phys.* 9 (2007) 1837.
- S. Gruegeon, S. Laruelle, L. Dupont, J.M. Tarascon, *Solid State Sci.* 5 (2003) 895.
- W. Luo, X. Hu, Y. Sun, Y. Huang, J. Mater. Chem. 22 (2012) 8916.
- B. Wang, J.L. Cheng, Y.P. Wu, D. Wang, D.N. He, *Electrochim. Commun.* 23 (2012) 5.
- F.X. Wang, S.Y. Xiao, X.W. Gao, Y.S. Zhu, Y.P. Wu, R. Holze, *J. Power Sources* 242 (2013) 560.
- Z.H. Li, T.P. Zhao, X.Y. Zhan, D.S. Gao, Q.Z. Xiao, G.T. Lei, *Electrochim. Acta* 55 (2010) 4594.
- K.E. Aifantis, T. Huang, S.A. Hackney, T. Sarakonsri, A.S. Yu, *J. Power Sources* 197 (2012) 246.
- J. Xie, G.S. Cao, Y.D. Zhong, X.B. Zhao, *J. Electroanal. Chem.* 568 (2004) 323.